Research article
doi.org/10.1002/elsa.202100125

Chemistry Europe
European Chemical Societies Publishing

Received: 15 June 2021
Revised: 21 July 2021
Accepted: 22 July 2021

Anti-corrosive additives for alkaline electrolyte in Al-air batteries: NH_4VO_3 and polyoxometalates

Anyie P. Atencio[1] | **Juan Ramón Aviles**[2] | **Dayatri Bolaños**[1] | **Roberto Urcuyo**[1] | **Mavis L. Montero**[3] | **Diego González-Flores**[1] | **Pilar Ocón**[2]

[1] Centro de Electroquímica y Energía Química (CELEQ), Centro de Investigación en Ciencia e Ingeniería de Materiales (CICIMA) y Escuela de Química, Universidad de Costa Rica, San José, Costa Rica

[2] Facultad de Ciencias, Universidad Autónoma de Madrid, Madrid, Spain

[3] Centro de Investigación en Ciencia e Ingeniería de Materiales (CICIMA) y Escuela de Química, Universidad de Costa Rica, San José, Costa Rica

Correspondence
Diego González-Flores, Centro de Electroquímica y Energía Química (CELEQ), Centro de Investigación en Ciencia e Ingeniería de Materiales (CICIMA) y Escuela de Química, Universidad de Costa Rica, 11501 2060 Sabanilla de Montes de Oca, San José, Costa Rica.
Email: diegoandres.gonzalez@ucr.ac.cr

Funding information
Vicerrectoría de Investigación, Universidad de Costa Rica; Consejo Nacional de Rectores

Abstract

Aluminum-air batteries are a promising alternative for portable energy storage. However, one of the significant issues in this technology is the corrosion of aluminum in alkaline electrolytes. In this study, we explored heteropolyacids (HPAs) $H_5PMo_{11}Al_{0.5}V_{0.5}O_{40}$ and $H_6PMo_{11}AlO_{40}$ as possible anti-corrosive additives in Al7475, Al6062, and Al5052 commercial alloys. We also investigated the anti-corrosive properties of commercial NH_4VO_3 and ZnO. Concerning HPAs, only $H_6PMo_{11}AlO_{40}$ in combination with Al5052 showed anti-corrosive activity. However, ZnO did not present anti-corrosive properties in Al6062 alloy, while NH_4VO_3 presented anti-corrosive properties for all three alloys. The combination of carboxymethylcellulose with NH_4VO_3 further improved the anti-corrosive properties in the Al7475 alloy. We observed by using 2D Raman imaging the formation of polymeric forms of tetrahedral $V^{+5}O_4$ over the surface of three alloys. The main conclusion of our studies is that NH_4VO_3 combined with carboxymethylcellulose is a promising anti-corrosive in the alkaline electrolyte of aluminum-air batteries.

KEYWORDS
alloys, aluminum, batteries, corrosion, energy storage

1 | INTRODUCTION

The rising of renewable energy around the entire planet requires new methodologies for energy conversion and storage. Batteries will definitively play a vital role in the energy handling paradigm for the next decades.[1,2] In that context, lithium batteries have been the front runner of all battery technologies, especially for portable applications such as electronic devices and electric vehicles.[3,4] However, in the past decade, commercial lithium batteries have not appreciably increased their capacity.[5,6] For that reason, the search for post lithium technologies with improved capacity has become of interest for future energy applications.

Aluminum-air batteries have a series of outstanding characteristics (cell voltage of 2.4 V in an alkaline electrolyte and high theoretical energy density of 8076 Wh/kg), which makes them attractive candidates for post lithium batteries, such as the ones used in electric vehicles (EVs).[7] Aluminum has four times more volumetric capacity than

Research article
doi.org/10.1002/elsa.202100125
Chemistry Europe
European Chemical Societies Publishing

lithium (8.0 versus 2.0 Ah/cm^3), and their mass capacity is similar (3.0 and 3.8 mAh/g for Al and Li, respectively).[8,9] Therefore, a car with a battery based on aluminum could have two to six times more travel range with the same volume. Aluminum has other praises compare to lithium, such as its recyclability, abundance, and price. In an aqueous medium and neutral pH, aluminum suffers passivation of the surface, which usually goes to the detriment of the battery's potential and current.[10,11] For that reason, it is usually preferable to use alkaline electrolytes. In general, the net anodic reaction of the battery in alkaline solution is:

$$Al + 3OH^- \rightarrow Al(OH)_3 + 3e^- \quad (1)$$

One of the significant challenges to overcome in this technology is the corrosion of the aluminum anode. In an alkaline medium, aluminum-air batteries lose much of their useful energy in a secondary reaction (self-corrosion) due to the reduction of water over the Al anode that leads to the evolution of H_2 (Equation 2),

$$Al + 3H_2O + OH^- \rightarrow Al(OH)_4^- + H_2 \uparrow \quad (2)$$

Two approaches can be used to avoid corrosion of aluminum. The first one is to use pure aluminum with minimal amounts of other elements such as Ga, In, Pb, Mg, Ca, Sn, Zn, Mn, Hg, and Cd.[12] These alloying elements have high hydrogen overpotential and therefore help to reduce hydrogen evolution and self-corrosion. The second strategy consists of modifying the electrolyte by adding additives that function as corrosion inhibitors.[13,14] The utilization of pure aluminum in this application is costly; therefore, it is better to implement commercially available aluminum alloys.[15] The use of anti-corrosive additives has been deeply studied to improve these alloy capacities by placing them as a versatile and low-cost alternative.

One of the most used anti-corrosive in alkaline electrolytes for aluminum-air batteries is zinc oxide; even though it has some disadvantages, such as low solubility in alkaline electrolytes and it tends to form a thick spongy layer over the electrode.[16] Different studies have proposed that the mechanism of inhibition involves the formation of zincate and metallic zinc species. It is well-known that ZnO works as an anti-corrosive additive for Al7475 and Al5052 alloys.[15,17] Moreover, zinc oxide, ZnO, has been used in conjunction with organic compounds such as polyethylene glycol.[18] The combination of ZnO and carboxymethyl cellulose (CMC) for Al5052 alloy in an alkaline medium resulted in a synergistic effect with a considerable decrease in the evolution of H_2. Some other organic compounds that have been used are plant extracts,[19] oil,[20] methanol,[21] agar,[22] carboxylic acids,[23] L-aspartic mixed with CaO,[24] and L-cysteine combined with cerium.[25]

The most effective inhibitors of corrosion for aluminum alloys are hexavalent chromates compounds.[26–28] However, since chromate is very polluting for the environment, chromate-like oxoanions such as molybdates, permanganates, tungstates, and vanadates are currently being studied.[29,30] Several studies are useing NH_4VO_3 as an anti-corrosive additive at near-neutral pH in different aluminum alloys.[31] NH_4VO_3 has been tested in AA7075, and AAl6061 and it shows very interesting anti-corrosive properties.[32,33] Nevertheless, it has not been implemented as anti-corrosive in alkaline electrolytes used in aluminum-air batteries. For that reason, we decide to study the compound NH_4VO_3 in strongly alkaline conditions. To find novel and more versatile anti-corrosive additives for aluminum-air batteries, in this study, we decided to test the anti-corrosive activity of an heteropolyacid (HPA) that contains vanadium in its structure $H_5PMo_{11}Al_{0.5}V_{0.5}O_{40}$ named from now on $PMo_{11}AlV_{0.5}$. HPAs are known to be firmly adsorbed on surfaces, which is interesting for anti-corrosive layers.[34–36] We also prepared the compound $H_6PMo_{11}AlO_{40}$ that we named $PMo_{11}Al$. This compound is very similar to $PMo_{11}AlV_{0.5}$ but without vanadium. HPAs are being investigated and used in multiple fields, and some analogous compounds have already been tested as additives in redox flow batteries.[30,37] However, to the best of our knowledge, no studies use them as anti-corrosive additives for aluminum alloys. We also tested the combination of NH_4VO_3 with CMC to study if there is a synergistic effect similar to the ZnO case.

In this work, we used three commercial alloys to test the additive's anti-corrosive activity: Al7475, Al6062, and Al5052, in which major alloying elements are zinc, silicon-magnesium, and magnesium, respectively. We performed different corrosion experiments such as hydrogen evolution, corrosion rate, polarization plots, impedance, and 2D Raman imaging to determine the best combinations of additive-alloy for aluminum-air battery prototypes.

2 | RESULTS AND DISCUSSION

2.1 | Hydrogen evolution test

The evolution rate of hydrogen and corrosion data for the different alloys exposed to 2 mol/L KOH solutions containing the mentioned additives are shown in Figure 1. KOH solutions in this concentration or higher are used to ensure high ionic conductivity for alkaline aluminum-air battery applications.[38] In the corrosion experiments, high HPAs concentrations are avoided in order to preserve the compounds and taking into account its high molecular

Research article
doi.org/10.1002/elsa.202100125
Chemistry Europe
European Chemical Societies Publishing

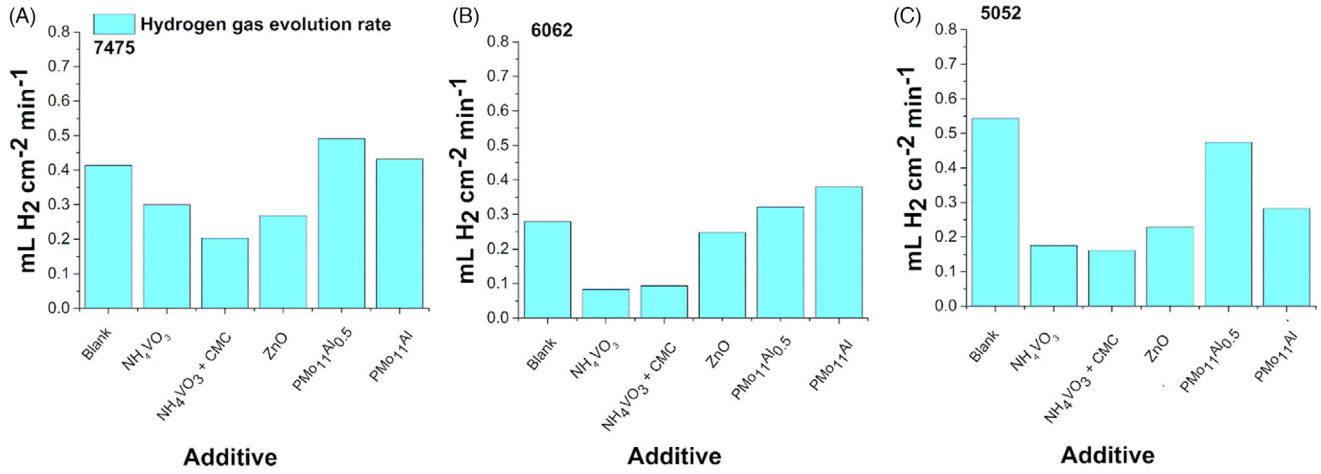

FIGURE 1 Hydrogen production measurements in 2 mol/L KOH for aluminum alloys: (A) 7475, (B) 6062, and (C) 5052. The corresponding raw measurements are shown in the Supporting Information (Figure S1). Concentrations of additives in alkaline solutions were NH_4VO_3 0.5 mol/L, ZnO 0.025 mol/L, $PMo_{11}AlV_{0.5}$ 10 mmol/L, $PMo_{11}AlV_{0.5}$ 10 mmol/L, NH_4VO_3 0.5 mol/L + CMC 10 g/L

TABLE 1 Chemical compositions of the different grades of commercial aluminum alloys (wt%)[41]

Alloy	Zn	Mg	Si	Cr	Fe	Mn	Cu
7475	6.20	2.60	0.10	0.25	0.12	0.06	1.90
6062	0.25	1.20	0.80	0.14	0.70	0.15	0.40
5052	0.10	2.80	0.25	0.35	0.40	0.10	0.10

weight. The solubility of ZnO limited the concentration of the ZnO solutions at this pH. On the other hand, NH_4VO_3 is very soluble and can be used in high concentrations. We decided to use 0.5 mol/L NH_4VO_3 according to the experiments we performed in batteries (Table S1). It is essential to mention that in different studies, Na_2SO_4 is used as an anti-corrosive additive in aluminum alloys. However, in tests not shown here, we observed that Na_2SO_4 increased twice the corrosion rate in Al 5052 alloys. For that reason, the study with these inhibitors was not included.

It is essential to keep in mind that hydrogen evolution is related to reaction (2). This reaction results in alloy corrosion and is strongly dependent on the intermetallic elements present in them. Figure 1 shows that the corrosion in 2 mol/L KOH without additive (intrinsic parasitic corrosion) is different for every alloy with the order Al5052 > Al7475 > Al6062. Some studies have shown that corrosion in aluminum alloys is strongly dependent on the content of different allowing elements such as magnesium.[39,40] According to Table 1, the content of magnesium in the aluminum alloys also shows the same trend as the intrinsic parasitic corrosion, which is Al5052 > Al7475 > Al6062. However, we cannot discard that other alloying elements such as zinc and iron also play an essential role.

When we study the influence of additives, it is observed that from the HPAs effect only $PMo_{11}Al$ showed a significant decrease in the rate of corrosion and evolution of hydrogen in Al5052 alloy. For that reason, we will focus mainly on NH_4VO_3, CMC, and ZnO additives in the rest of the study.

Al7475: the NH_4VO_3 + CMC solution produces a more significant decrease in the evolution of H_2 compared with the rest of the additives, followed by the ZnO and the NH_4VO_3.

Al6062: the evolution of H_2 and corrosion rate are clearly reduced when the additive used is NH_4VO_3; its effectiveness is only comparable with the combined action of NH_4VO_3 + CMC. Interestingly, ZnO does not appreciably decrease the H_2 production rate.

Al5052: this alloy is also very susceptible to the additives; NH_4VO_3 and NH_4VO_3 + CMC lead to an appreciable decrease in the evolution of H_2. ZnO also significantly decreases the H_2 generation reaction.

It is crucial to notice that NH_4VO_3 and NH_4VO_3 + CMC were the most versatile anti-corrosive additives, having an important effect on the three alloys. However, the strength of the effect of the additive is also dependent on the alloy. For example, in Al7475, NH_4VO_3 and NH_4VO_3 + CMC decrease the hydrogen evolution by 28% and 51%, respectively. In Al5052, the effect was even stronger; NH_4VO_3 and NH_4VO_3+CMC decreased hydrogen evolution by over 68%. In Al6062, NH_4VO_3 and NH_4VO_3+CMC decrease the hydrogen evolution by 70% and 66%, respectively. The dependency on the alloy and its interaction with the corrosive additives in the factors affecting the parasitic corrosion through reaction (2) show its complexity.

Kharitonov et al.[28,42,43] studied the anti-corrosive effect of $NaVO_3$ in Al6063 near to neutral pH using Raman

Research article
doi.org/10.1002/elsa.202100125
Chemistry Europe
European Chemical Societies Publishing

imaging and XPS experiments. Based on their experiments, they proposed an inhibition mechanism. They suggested intermetallic species on the aluminum alloy surface, such as magnesium, in function of the cathodic sites that can reduce V^{+5} species forming V^{+4} monomers over them. The mixture of V^{+5}/V^{+4} can later polymerize due to the local acidification from anodic dissolution. This polymerized film can initially be amorphous, but it can become crystalline if the polymerization and condensation continue. If, after several hours, the crystalline film continues to grow in thickness, sometimes it cracks and breaks down, diminishing in this way the protection of the surface.[42] They also mention that V^{+5} monomers and oligomers can be formed on the surface of the Al, resulting in anodic inhibition; however, this film is much thinner than the one formed over the intermetallic particles.

In our experiments, the anti-corrosive effect of NH_4VO_3 in alkaline conditions was studied, because they are more suitable for aluminum-air batteries. To better understand the interaction between anti-corrosive additives and the alloys' surface, we performed 2D Raman imaging experiments in samples that were immersed in a 2 mol/L KOH solution with 0.5 mol/L NH_4VO_3 for 1.5 h (Figure 2). It is known that in an alkaline medium, vanadate is tetrahedral with an oxidation state V^{+5} (VO_4^{3-}, $V_2O_7^{-4}$, and $(VO3)_n^{-n}$).[44,45] However, if local acidification of anodic sites is carried out on the metal surface, hydrolysis of dissolved metal ions occurs, which leads to the polymerization of polyvanadate ions.[42] We hypothesize that magnesium intermetallic particles can have a similar cathodic effect in our alloys, reducing V^{+5} to V^{+4} species. For this reason, we expect a very similar species form and a similar corrosion inhibition mechanism in our films like the one proposed by Kharitonov. However, the analysis of the Raman peaks for vanadium species is complicated since their shape or position can change due to several factors:

- Ionic strength: it can increase or decrease the number of oligomers, thereby the frequencies observed.
- Oxidation state: vanadium +4 species have lower bond strength compared to vanadium +5 species.
- The mixture of polymeric and crystalline species can make different peaks overlap and shift. In general, amorphous polymeric peaks are broader and rounder meanwhile crystalline peaks are sharper and narrower.

The results of our 2D Raman imaging experiments are shown in Figure 2. The Al7475 alloy shows the formation of flakes that we also observed in Figure 2A. The broad band at 868 cm^{-1} in the blue spectrum (Figure 2B) corresponds to tetrahedral polymeric species of vanadium, containing a mixture of V^{+5} with a smaller portion of V^{+4}; meanwhile, the band at 939 cm^{-1} corresponds to the distorted V^{+4} = O stretching mode.[46] The green spectrum (Figure 2C) shows sharp peaks at 852 cm^{-1}, 815 cm^{-1}, 334 cm^{-1}, and 267 cm^{-1}, which are common to some polymeric V^{+5}–Mg species such as $Mg_4V_2O_9$ or $Mg_3(VO_4)_2$ phases.[47] These data suggest that vanadium has to penetrate through the flake boundary, where it forms intermetallic species with magnesium and polymerizes to the interior of the flakes' structure.

The Al6062 alloy in the blue spectrum (Figure 2H) also shows a broad band at 878 cm^{-1} that corresponds to tetrahedral polymeric species of V^{+5}. The green spectrum (Figure 2I) shows a band at 896 cm^{-1} and 848 cm^{-1} corresponding to $V^{+4/+5}$ = O symmetric and asymmetric modes in crystalline polymeric species. The band at 505 cm^{-1} in the red spectrum (Figure 2J) is typical of aluminosilicates.[48,49] These aluminosilicates usually have the formula $Al_{4.01}XSi_{0.74}$, where X can be Mn or Na.[48,50] This kind of aluminosilicates is known to form an anti-corrosive protective layer over aluminum alloys.[49,51–53]

The green spectrum in the Al5052 alloy (Figure 2F) also shows peaks at 867 and 337 cm^{-1}, which are observed in some polymeric V^{+5}–Mg species and suggest the presence of $Mg_4V_2O_9$ or $Mg_3(VO_4)_2$ intermetallic phases over the Al5052 alloy, but more amorphous than in the case of the Al7475 alloy. It also shows a broad band at 889 cm^{-1} (Figure 2E) corresponding to tetrahedral polymeric species of V^{+5}. Both species are homogeneously distributed over the surface of the alloy.

In the Al6062 alloy, the formation of an anti-corrosive aluminosilicate layer over the electrode seems to be intrinsic to the nature of the alloy that contains a high amount of silicon. This protective layer formation could explain why this alloy is more resistant to corrosion when no anti-corrosive additives are used. We observed that tetrahedral polymeric species of V^{+5} were common to the three alloys and probably play a fundamental role in the anti-corrosive activity. However, it is clear that depending on the alloy, other species are formed, like intermetallic compounds with magnesium (or aluminosilicates in Al6062). This adds complexity to the analysis of the anti-corrosive activity since other factors might play an important role, such as the morphology and stability of the formed film. However, in general terms, we observed very similar species as in the study of Kharitonov et al.,[42] suggesting that the protection mechanism is similar.

2.2 | Polarization curve measurements

Concerning the polarization plots measurements (Figure 3), the anodic current obtained is related to aluminum dissolution according to Equation 1; meanwhile,

Research article
doi.org/10.1002/elsa.202100125
Chemistry Europe
European Chemical Societies Publishing

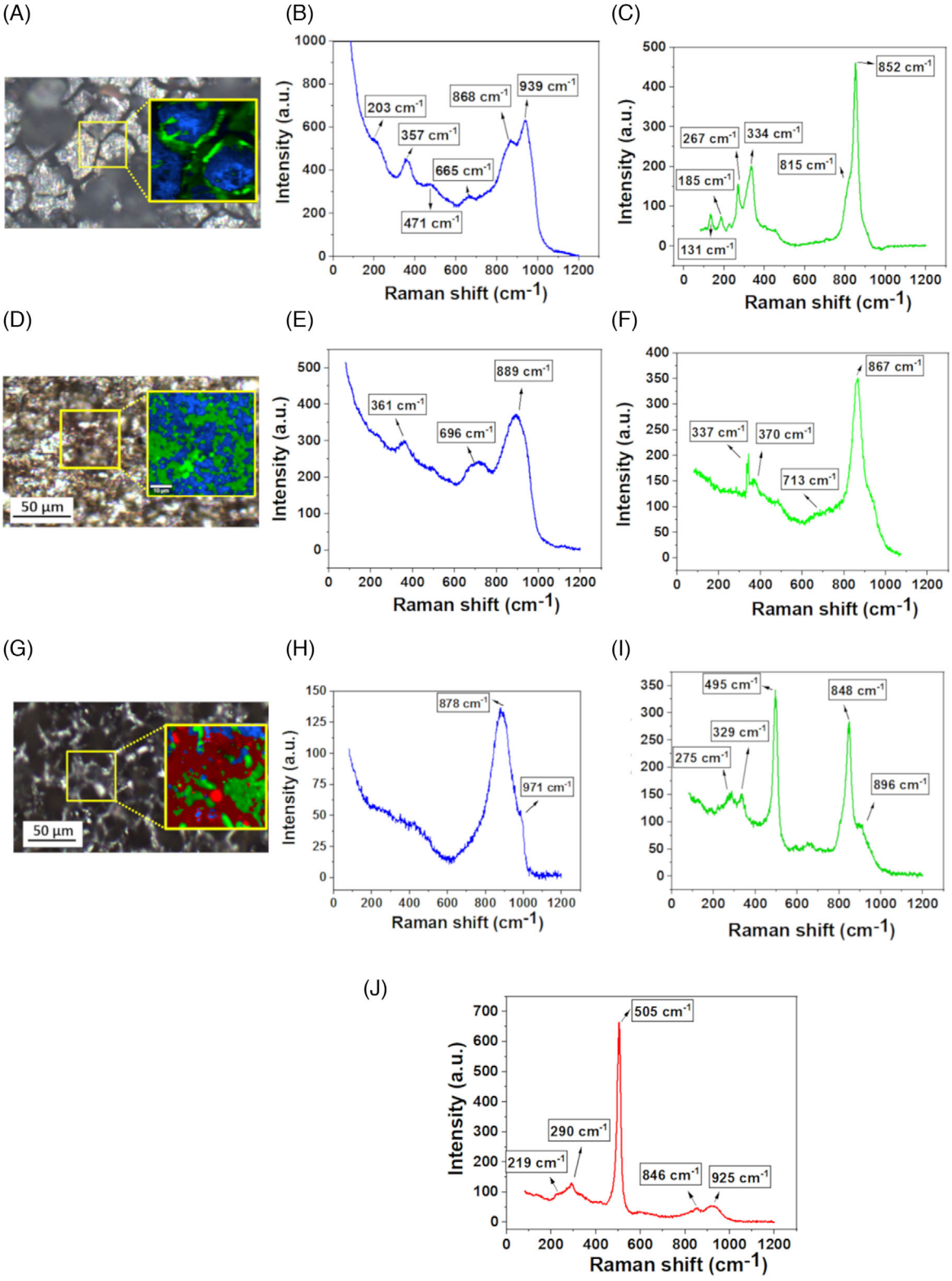

FIGURE 2 Raman 2D imaging of alloys after exposure for 1.5 h to a 2 mol/L KOH solution with 0.5 M NH_4VO_3 for (A) Al7475, (D) Al5052, and (G) Al6062. Every color in the Raman image corresponds to the Raman spectrum of the same color and represents the distribution of that species on the surface of the alloy. The scale bar in all micrographs is 50 µm

Research article
doi.org/10.1002/elsa.202100125
Chemistry Europe
European Chemical Societies Publishing

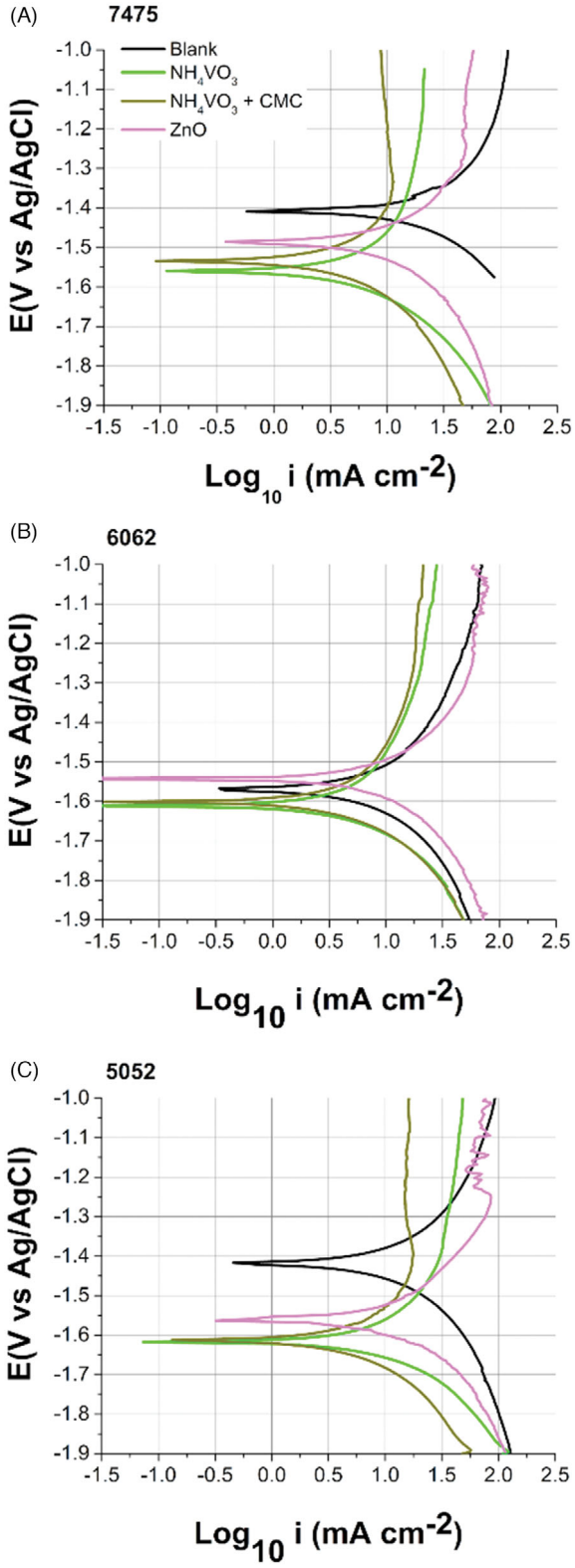

FIGURE 3 Polarization plots in 2 mol/L KOH and scan rate 0.5 mV/s for aluminum alloys (A) 7475, (B) 6062, and (C) 5052

the cathodic current is related to oxygen reduction according to Equation 3 and/or water reduction according to Equation 4.

$$O_2 + 2H_2O + 4e^- \rightarrow 4OH^- \quad (3)$$

$$2H_2O + 2e^- \rightarrow 2OH^- + H_2 \quad (4)$$

It is essential to clarify that the corrosion current (i_{cor}) obtained by polarization plots is not directly related to the parasitic corrosion occurring through Equation 2. As we mentioned before, the hydrogen evolution reaction occurs in the aluminum electrode interface and does not produce current. On the other hand, the corrosion current obtained by polarization plots is related to Equation 1 and describes how easily aluminum can be oxidized to deliver current. When an additive increases the corrosion current (i_{cor}) concerning the black, the additive favors the dissolution of aluminum. On the contrary, when an additive decreases the corrosion current (i_{cor}), this indicates aluminum dissolution inhibition. If an additive decreases the parasitic corrosion (Equation 2) and decreases the corrosion current (Equation 1), even though the alloy will undergo less dissolution through hydrogen evolution, it will also deliver less current. However, if the alloy will be used in an aluminum-air battery that does not require a high current or high power, the partial inhibition of the corrosion current (Equation 1) should not be a significant problem in the battery's performance.

Tables 2–4 compare the corrosion parameters obtained from the hydrogen evolution tests (i_{H2}) and polarization measurements (i_{corr}). In the study by Zhu et al., they observed that the corrosion rate results for aluminum using different methodologies are not necessarily consistent in magnitude, but they are consistent in trend.[17]

The values calculated for the anodic (βa) and cathodic (βc) Tafel slopes as well the percentage of inhibition (ηa%) found for each additive are detailed in Table S2–S4.

Al7475: the highest ηa% was 72%, corresponding to the solution containing NH_4VO_3 + CMC, followed by ZnO and NH_4VO_3 with 53 both respectively.

The βa and βc of the solutions with NH_4VO_3 changed compared the blank (βc Blank: −162 mV/ βc NH_4VO_3: −250 mV, βa Blank: 176 mV/βa NH_4VO_3: 409 mV), revealing that vanadate cannot be classified as a single type of inhibitor because its strong combined effect that suppresses the cathodic reaction and slows the dissolution of aluminum. The effect of NH_4VO_3 + CMC on Tafel slopes also suggests a mixed effect.

Al6062: the NH_4VO_3 has a ηa% of 58%, followed by NH_4VO_3 +CMC (46%). The polarization curves of Al6062 supports the mixed effect of NH_4VO_3 and NH_4VO_3 + CMC inhibitors for this alloy, partially tending to suppress the cathodic reaction. Meanwhile, it is observed that

Research article
doi.org/10.1002/elsa.202100125
Chemistry Europe
European Chemical Societies Publishing

TABLE 2 Corrosion parameters for Al7475 alloy

Additive	Hydrogen gas evolution rate (mL cm^{-2} min^{-1})	I_{H2} (mA/cm^2)	$E_{corr}/V_{vsAg/AgCl}$	i_{corr} (mA/cm^2)
Blank	0.414	51.42	−1.411	13.30
NH_4VO_3	0.300	42.06	−1.538	6.20
NH_4VO_3 + CMC	0.203	24.65	−1.538	3.65
ZnO	0.268	29.00	−1.485	6.28

TABLE 3 Corrosion parameters for Al6062 alloy

Additive	Hydrogen gas evolution rate (mL cm^{-2} min^{-1})	I_{H2} (mA/cm^2)	$E_{corr}/V_{vsAg/AgCl}$	i_{corr} (mA/cm^2)
Blank	0.279	31.87	−1.577	12.21
NH_4VO_3	0.083	10.62	−1.609	5.19
NH_4VO_3 + CMC	0.094	10.04	−1.579	6.56
ZnO	0.247	27.93	−1.545	9.79

ZnO strongly suppresses anodic kinetics and can influence the cathodic reaction. These mixed inhibition results for Al6062 are consistent with previous reports.[17,54]

Al5052: the solutions with NH_4VO_3 and NH_4VO_3 + CMC had 46 and 59% inhibition percentages, respectively, followed by ZnO (12%). In the Al5052 alloy, NH_4VO_3, NH_4VO_3 + CMC and ZnO showed a strong effect in the anodic kinetics (βa Blank: 389 mV, βa NH_4VO_3: 460 mV, βa NH_4VO_3+CMC: 576 mV, βa ZnO: 324 mV).

In general, only in the Al7475 alloy, the combination NH_4VO_3 + CMC improved the inhibition compared to NH4VO3 alone. Moreover, we observed that additives that inhibit parasitic corrosion through Equation 2 (hydrogen evolution) usually also inhibit corrosion through aluminum's dissolution (Equation 1). This typically happens because the protective layer blocks the surface suppressing of both reactions. (see polarization curves in Figure S2). For this reason, we did not test higher metavanadate concentrations since further inhibition of reaction 1 will go to the detriment of the batterie's current. We will publish a more detailed study on this topic.

2.3 | Open circuit potential

The change in the open circuit potential (E_{OCP}) of the alloys in solutions with additives shows the effect of the anti-corrosive decreasing the corrosion current density (i_{corr}).[32] This decrease in the current is related to an inhibition in the cathodic kinetics or the anodic reaction in the electrode (a change of 85 mV in the E_{OCP} toward one or the other direction). If the change does not exceed this threshold value of ±85 mV, then the inhibitor is classified as a mixed type. In our system, both the anodic dissolution of Al (Equation 1) and the cathodic reduction of O_2 or H_2O (Equations 3 and 4) can be affected.

The open-circuit potentials for each alloy-additive combination are tabulated in Table S5. However, a summary of the shifting in the OCP values regarding the black sample is shown in Figure 4. The hydrogen evolution measurements showed that HPAs did not help with the anti-corrosive activity except for one combination $PMo_{11}Al$ with Al5052 alloy, which showed a mixed inhibitory effect in the OCP of the polarization plots. We still do not fully understand the mechanism for this inhibitory effect. However, from the practical point of view, we decided to focus on the inhibitory effect of NH_4VO_3 based additives, which would have more possibilities to be used in the batteries market because it is cheaper and commercially available.

Al7475: The blank solution of this alloy had an E_{OCP} −1,404 $V_{vsAg/AgCl}$, which moved to more positive values (E_{OCP} −1,304 V and −1.321 V) in the solutions of HPAs.This suggests that these two additives modify the dissolution

TABLE 4 Corrosion parameters for Al5052 alloy

Additive	Hydrogen gas evolution rate (mL cm^{-2} min^{-1})	I_{H2} (mA/cm^2)	$E_{corr}/V_{vsAg/AgCl}$	i_{corr} (mA/cm^2)
Blank	0.543	71.97	−1.427	20.47
NH_4VO_3	0.175	19.26	−1.619	11.03
NH_4VO_3 + CMC	0.161	16.83	−1.615	8.40
ZnO	0.228	24.86	−1.558	13.44

Research article
doi.org/10.1002/elsa.202100125
Chemistry Europe
European Chemical Societies Publishing

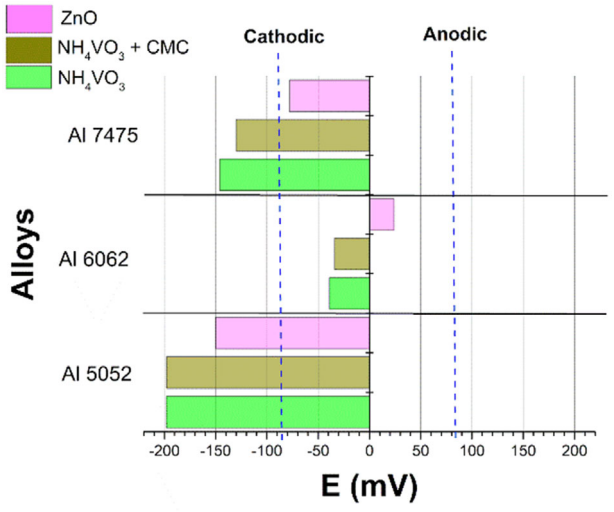

FIGURE 4 Displacement of Ec_{orr} in the cathodic or anodic direction for alloys in solutions with additives. The potential value corresponds to the subtraction of the blank samples' OCP from the samples' OCP values. Dashed lines indicate ±85 mV

mechanism of aluminum. Regarding ZnO, NH_4VO_3, and NH_4VO_3 + CMC, the change was toward more negative. The E_{OCP} values shift due to the additives' anti-corrosive effect and suppressing the cathodic kinetics in the electrode.

Al6062: This is a particular case because none of the additives change the E_{OCP} beyond the reference value (±85 mV). It seems the additives affect both reactions to some extent (mixed effect). In detail, both NH_4VO_3 and NH_4VO_3 + CMC slightly change the OCP in the cathodic direction while the rest of the additives produce a shift in the anodic direction.

Al5052: NH_4VO_3, NH_4VO_3 + CMC, and ZnO are all cathodic inhibitors (E_{OCP} −1,612V, 1,612V, and −1,564 V) (Table S5).

In general, we observed that the response of the **Al7475** alloy to the additives was more complicated than for the other alloys. The shift in OCP was cathodic for NH_4VO_3, ZnO, and NH_4VO_3+CMC. We also measured the OCP for solutions with CMC as an inhibitor and observed a similar shift in the OCP as in NH_4VO_3+CMC.

The corrosion inhibition of aluminum using organic compounds is well established. Polar groups with nitrogen, oxygen, and sulfur atoms are responsible for the inhibitory effect by forming strong coordination bonds. The water molecules on the metal surface are replaced by organic molecules that can interfere with the anodic and cathodic reactions on the metal. It has been predicted that factors such as electron density at the donor site, molecular weight, and steric hindrance are some characteristics that influence inhibitor performance.[13] However, the exact operating mechanisms for this type of additives are still under debate.

ZnO's inhibitory properties could be explained by the fact that ZnO in a highly alkaline solution takes its zincate form and then forms metallic zinc according to Equations (5) and (6).

$$ZnO + H_2O + 2OH^- \rightarrow Zn(OH)_4^{2-} \quad (5)$$

$$3Zn(OH)_4^{2-} + 2Al \rightarrow 3Zn + 2Al(OH)_4^- + 4OH^- \quad (6)$$

Hydroxides compose the layer formed by ZnO and metallic zinc deposits that form a galvanic pair with aluminum. The characteristic porous layer is shown in Figures S4-S9.

The **Al6062** alloy has the most negative OCP in 2 mol/L KOH from the three alloys (Table S4), which results in the alloy with lower intrinsic corrosion. This highly negative OCP value also makes the alloy less susceptible to the effect of the different additives. As it can be seen in Figure 4, all additives produce a shift lower than ±85 mV in the OCP, which accounts for a mixed inhibitory effect in all of them. Surprisingly, in the ZnO additive, this mixed-anodic shift results in no significant corrosion inhibition.

Finally, we have the **Al5052** alloy, which is the one that initially has the highest hydrogen evolution rate and corresponds to the lower quality alloy in terms of corrosion resistance. We can observe that the three main additives, ZnO, NH_4VO_3, and NH_4VO_3+CMC, result in strong corrosion inhibition and a solid cathodic shift in the OCP (Figure 4). It is crucial to notice that the use of NH_4VO_3 based inhibitors allow the leveling of alloys like Al5052 with less resistance towards corrosion and make them similar to more corrosion-resistant alloys like Al6062.

2.4 | Surface analysis

SEM images for the main alloy-additive couples are shown in Figure 5. Samples were measured after the hydrogen evolution test.

Al7475: The blank sample shows the formation of a thick layer upon corrosion composed of flakes. In general, the blank sample surface (Figure 5A) after corrosion contains Mn, Cu, Zn, and Fe intermetallic elements. The sample treated with the NH_4VO_3 additive (Figure 5B) shows a very similar structure to the blank sample, but it has incorporated vanadium on its composition. The structure in the sample treated with ZnO additive (Figure 5C) is different. In this case, the zinc oxide recovers the surface of the alloy, which is observed as a layer with a porous appearance (Figures S10–S13).

Research article
doi.org/10.1002/elsa.202100125
Chemistry Europe
European Chemical Societies Publishing

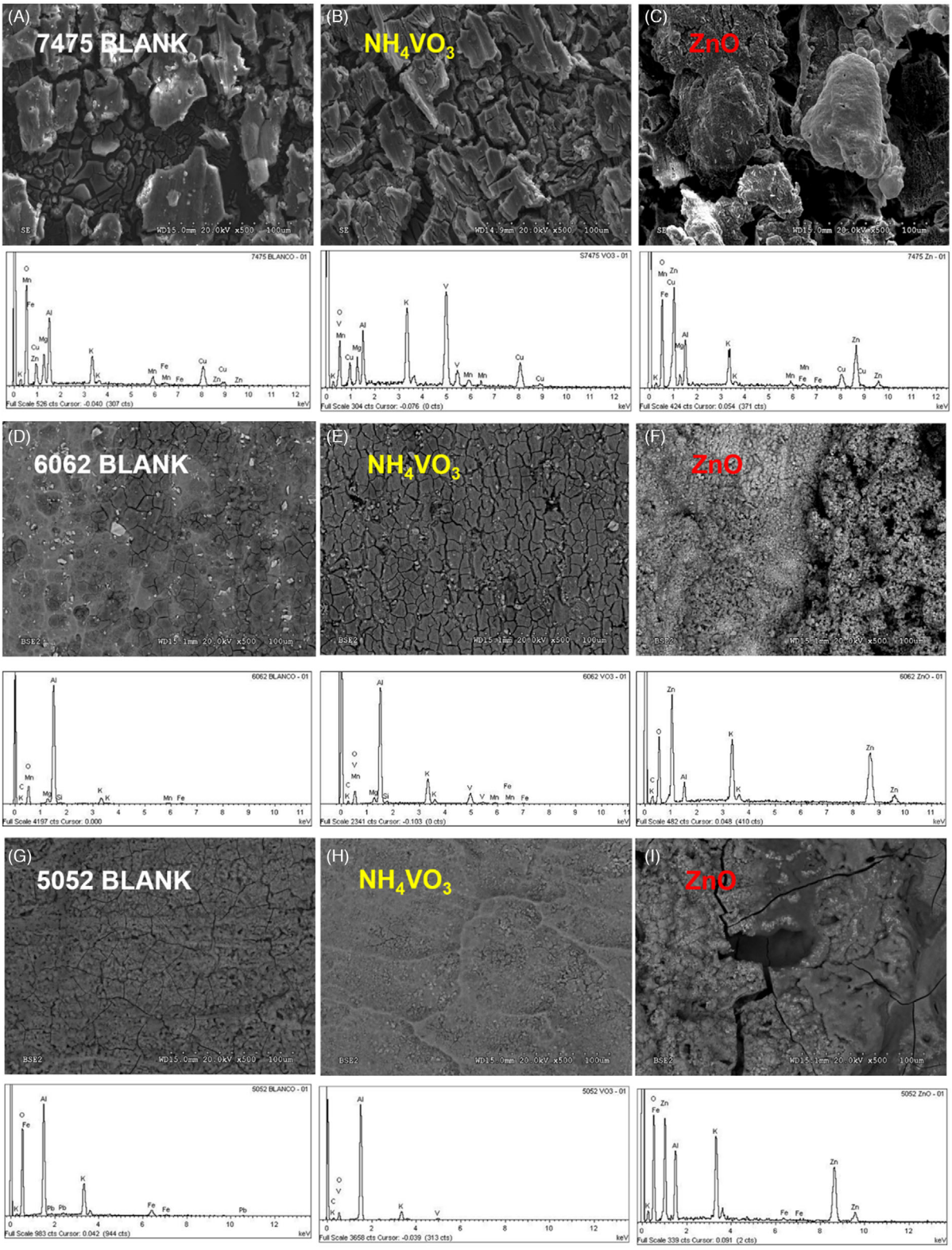

FIGURE 5 SEM images at 500 magnification after treatment for 30 minutes in the corresponding solutions for 7475 alloy, (A) blank in 2 mol/L KOH, (B) 2 mol/L KOH and 0.5 mol/L NH_4VO_3, and (C) 2 mol/L KOH and 0.025 mol/L ZnO, for 6062 alloy, (D) blank in 2 mol/L KOH, (E) 2 mol/L KOH and 0.5 mol/L NH_4VO_3, and (F) 2 mol/L KOH and 0.025 mol/L ZnO, for 5052 alloy, (G) blank in 2 mol/L KOH, (H) 2 mol/L KOH and 0.5 mol/L NH_4VO_3, and (I) 2 mol/L KOH and 0.025 mol/L ZnO

Research article
doi.org/10.1002/elsa.202100125
Chemistry Europe
European Chemical Societies Publishing

Al6062: The blank samples (Figure 5D) show the formation of a smoother surface than in the Al7475 alloy. The EDX analysis mainly showed traces of Mn and Fe intermetallic elements. The sample treated with the NH_4VO_3 additive (Figure 5E) shows the incorporation of vanadium on the surface of the alloy, which also contains flakes in the structure but of a much smaller size than in the case of the Al7475 alloy. Meanwhile, the sample treated with ZnO additive (Figure 5F) shows the formation of a porous zinc oxide layer over the alloy (Figures S14–S21).

Al5052: The blank sample (Figure 5G) also shows the formation of a smoother oxide surface than in the case of the Al7475 alloy. This layer contains Fe and Pb intermetallic elements. The sample treated with NH_4VO_3 additive (Figure 5H) shows an even smoother surface that contains vanadium in its composition. On the other hand, the samples treated with ZnO additive (Figure 5I) show a zinc oxide layer formation. However, in this case, the zinc oxide layer has a more compact appearance than the other two alloys.

In the three alloys, the HPAs solutions produce the addition of Mo and V on the surface and the grains, especially in the Al5052 (see Figures S22–S29).

2.5 | EIS measurements

The Nyquist plots for **Al7475**, **Al6062,** and **Al5052**, in blank solution and including NH_4VO_3, NH_4VO_3 + CMC, and ZnO, combinations as additives are shown in Figure 6. They consist of two parts: a high-medium frequency (10^5-50 Hz) capacitative loop caused by the charge transfer of the corrosion process. According to Brett, the first capacitive time constant corresponds to interfacial reactions of Al oxidation at the metal/oxide/electrolyte interface. In this process, the formation of Al^+ ions at the metal/oxide interface and their migration through the oxide layer to the oxide/solution interface occur due to high electric field strength, where they get oxidized to Al^{3+}.[55,56] The second capacitive loop appearing at low frequency could be originated from the growth and dissolution of the surface film.[57]

The equivalent circuit model can fit these Nyquist diagrams suggested and included in Figure 6. The obtained parameters were extracted from this model and summarised in Table 5. The model consists of an Rs (solution resistance), a series combination of a constant phase element (CPE1) in parallel with R_{ct1}(charge transfer resistance), and this in series with CPE2 in parallel with an R_{ct2} charge transfer resistance.

The model included constant phase elements (CPE) because of the depressed semicircles due to the inhomogeneity distribution (microscopic roughness) on the solid

TABLE 5 Fitting parameters obtained from the impedance measurements

Sample	Rs(Ω)	CPE1-T(+)	CPE1-P(+)	R_{ct1} (Ω)	CPE2-T(+)	CPE2-P(+)	R_{ct2} (Ω)	Rct1(+)+Rct2 = Rtotal (Ω)	$(R_{Tinh}-R_{TBlank})/R_{tinh}$ %
7475	5.12	5.50E−04	0.87	16.56	8.99E−04	0.90	3678	3695	
NH_4VO_3	4.1	5.20E−04	0.76	3.06	1.11E−04	0.92	6436	6616	44
NH_4VO_3 + CMC	3.00	5.35E−05	0.77	1.20	1.80E−04	0.92	5152	5153	28
ZnO	1.84	3.84E−04	0.87	1.32	1.91E−05	0.98	38767	25683	86
	Rs(Ω)	CPE1-T(+)	CPE1-P(+)	Rct1(Ω)	CPE2-T(+)	CPE2-P(+)	Rct2 (Ω)	Rct1(+)+Rct2 = Rtotal (Ω)	$(R_{Tinh}-R_{TBlank})/R_{Tinh}$
6062	2.05	1.30×10^{-04}	0.89	3.21	1.40×10^{-04}	0.99	27839	27842	
NH_4VO_3	4.28	2.90×10^{-04}	0.77	10.75	1.07×10^{-04}	1.00	10978	10989	−140
NH_4VO_3 + CMC	3.30	2.40×10^{-04}	0.79	4.87	1.05×10^{-03}	0.95	4843	4848	−444
ZnO	2.05	3.52×10^{-05}	1.01	0.54	1.75×10^{-04}	0.93	47152	47153	44
	Rs(Ω)	CPE1-T(+)	CPE1-P(+)	Rct1(Ω)	CPE2-T(+)	CPE2-P(+)	Rct2 (Ω)	Rct1(+)+Rct2 = Rtotal (Ω)	$(R_{Tinh}-R_{TBlank})/R_{Tinh}$
5052	2.07	8.57×10^{-05}	1.01	7.04	2.60×10^{-03}	0.85	270.2	277	
NH_4VO_3	4.19	2.50×10^{-04}	0.74	5.98	1.10×10^{-04}	1.01	13175	13181	98
NH_4VO_3 + CMC	3.17	1.85×10^{-04}	0.77	5.16	7.23×10^{-05}	1,1	20077	20082	99
ZnO	1.28	1.10×10^{-04}	0.75	3.80	1.20×10^{-04}	0.98	67765	67769	100

Research article
doi.org/10.1002/elsa.202100125
Chemistry Europe
European Chemical Societies Publishing

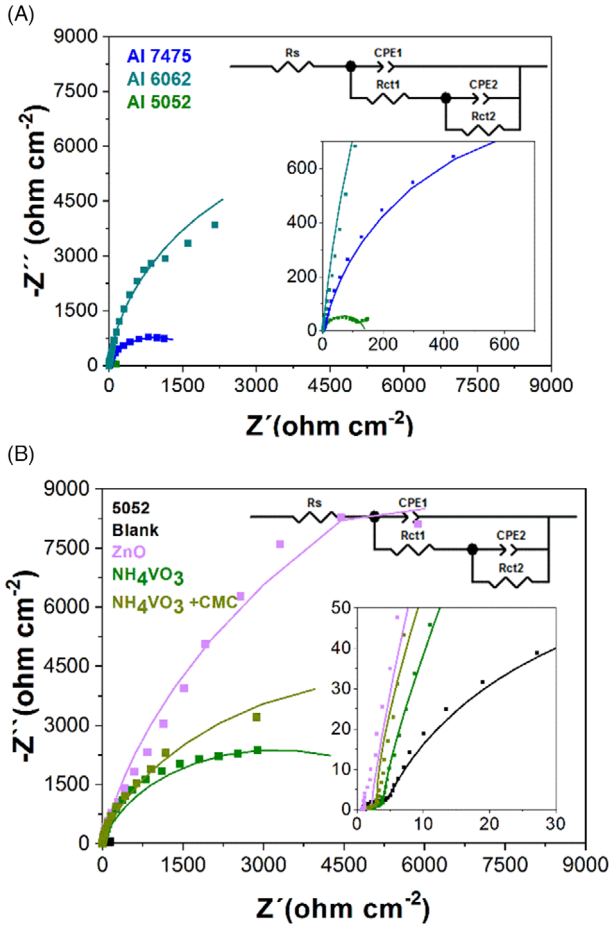

FIGURE 6 Nyquist plots of (A) 7475, 6062, and 5052 alloys in the corresponding blank solutions of 2 mol/L KOH, (B) 5052 alloy in the corresponding solutions with 2 mol/L KOH and ZnO 0.025 mol/L; 2 mol/L KOH and 0.5 mol/L NH_4VO_3; and 2 mol/L KOH with 0.5 mol/L NH_4VO_3 + 10 g/L CMC

electrode. The CPE used in equivalent circuit is defined by the components Q and n and is deduced by the following relation[58]:

$$Z_{CPE} = \left(\frac{1}{Q(j\omega)^n}\right) \quad (7)$$

where Q is the proportionality constant and comparable to capacitance, j is the imaginary unit, ω is the angular frequency, and n is phase shift and related to the degree of surface non-homogeneity. The value of n describes the CPE. The CPE represents resistance if (n = 0, Q = R), capacitance (n = 1, Q = C), and Warburg impedance (n = 0.5, Q = W). In the present study, the value of n varies from 0.74 to 1.00 in the presence of inhibitors indicating the similarity of CPE with capacitor when n is near to 1.

The impedance measurements for the blank samples are consistent with the hydrogen production measurements (Figure 6A). The total resistance of the samples

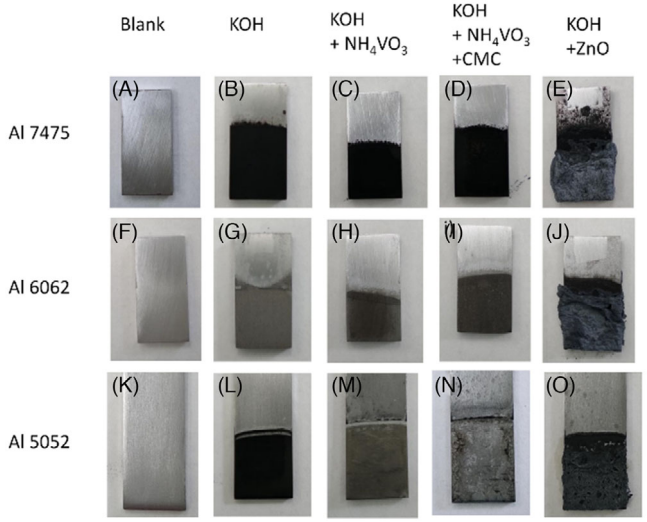

FIGURE 7 Alloy pieces after treatment in 2 mol/L KOH with different additives

(related to the corrosion rate) increases according to Al5052 > Al7475 > Al6062. Therefore, the Al5052 alloy corrodes much faster than the Al6062 alloy, according to the H_2 production experiments presented above.

The impedance measurements in the Al7475 alloy show that NH_4VO_3 and NH_4VO_3 + CMC result in corrosion protection compared to the blank (Figure S31a). The total resistance is increased from 3793 Ω in the blank sample to 6616 Ω and 5153 Ω in the NH_4VO_3 and NH_4VO_3 + CMC samples, respectively. However, ZnO shows higher total resistance than in the other alloys, which is again inconsistent with the hydrogen production tests. The corrosion process in the Al7475 alloy forms a thick oxide layer over the electrode that could fall and regrow (Figure 5A). The process becomes even more complex when NH_4VO_3 is added to the solution because an inhibitory layer based on the vanadium species also has to grow over the alloy. When NH_4VO_3 additives are used, the impedance behavior is also related to the nature of the protective layer over the electrode and how mechanically stable it is. The flakes formed over the electrode can likely peel off and avoid the formation of thick polymeric vanadate layers. This type of process in which an unstable layer is formed over the electrode has been observed previously.[45,53]

The impedance experiments with the **Al6062** alloy are very particular (Figure S31b). The Al6062 alloy naturally forms an effective anti-corrosive layer that cannot be easily removed, as observed in Figure 7G and Figure S30. As we observed in the Raman experiments, this layer consists of aluminosilicates with anti-corrosive properties. When NH_4VO_3 and NH_4VO_3 + CMC are added, the formation of this aluminosilicate layer is partially inhibited, and a vanadate layer is formed instead (Figure 7H and I).

This vanadate layer can be easily removed, as observed in Figure S30. Again, ZnO forms a very thick layer with very high resistance, as in the case of the Al5052 alloy.

Finally, **Al5052**: When the alloy is the blank electrolyte (KOH 2 M) the high-medium, and low-frequency loop shows that the material suffers a strong attach from alkaline solution (Figure 6B). The total resistance $R_{ct1}+ R_{ct2}$ is approximately 275 Ω, the CPE1 and 2 have n ~ 1-0.84. This resistance value in Al5052 with NH_4VO_3 and $NH4VO_3$ + CMC is much higher in comparison with the blank solution. The formation of a protective layer over the electrode seems to justify this result. With NH_4VO_3 additive, the impedance module increases significantly at low frequency. The total resistance goes 50 times higher than the blank solution (13.180 Ω) (see Table 5). The same behavior was found with NH_4VO_3 + CMC, although more pronounced. Impedance measurements with ZnO additive (Figure 6) are pretty different. The strong effect in the impedance module is carried out; the total resistance value now is 100 times higher than the blank solution. According to the EIS spectra, ZnO represents the best anti-corrosive additive. This behavior is inconsistent with the hydrogen production tests. A possible explanation could be the nature of the protective layer formed.

Figure 7E shows that ZnO produces a very thick amorphous layer over the electrode. This deposit could facilitate the formation of discharge layer film that limits mass diffusion. This thick layer results in an increased resistance but not necessarily in better protection toward corrosion. NH_4VO_3-based anti-corrosives result in a more compact layer over the electrode. However, it represents better anti-corrosive protection. This increased protection is possibly related to the close interaction of vanadate species with the intermetallic species of the alloys that we observed in the Raman experiments.

In general, we can say that the nature and chemistry of the protective layer formed by ZnO or NH_4VO_3 are very different, which makes it very difficult to directly compare them by impedance measurements because the observed resistance does not necessarily correlate with the hydrogen production experiments. NH_4VO_3 inhibitors do not require to form a very thick layer to be effective. In this case, it is more critical the close interaction of vanadate species with the surface of the alloy to form these thin layers of polymeric vanadate.

ZnO's protection mechanism is the formation of a spongy layer over the surface of the electrode. In the case of the NH_4VO_3 additive, the layer's behavior seems to be more complex and dynamic. Different types of vanadium species can be formed on the surface; this species can polymerize and crystallize, forming thicker and more unstable layers that can fall out and regrowth, but in general, remain thinner than the ZnO layers.

The thick deposits formed by the ZnO additive (Figure 7) could represent a problem when implemented in aluminum-air batteries. Different studies report a blocking effect of oxide by-products in the air cathode of metal-air batteries.[59–61] These oxides can come from the oxidation of aluminum or the ZnO additive itself. NH_4VO_3 additives, on the other hand, are very soluble and do not form any deposits, which represents an advantage over the ZnO additives. In the preliminary studies showed in Table S1, no apparent effects of NH_4VO_3 additives were observed on either the chemistry or the cathode performance. However, this is something that we will study in more detail in the future.

3 | CONCLUSION

POMs did not show anti-corrosive activity, except for $PMo_{11}Al$ mixed with Al5052 alloy. The polarization measurements showed a mixed anodic-cathodic mechanism. Understanding more about this additive will be interesting from a fundamental point of view. Nevertheless, it is possibly too expensive to be used in aluminum-air batteries.

The effect of ZnO anti-corrosive additive in Al alloys for battery applications has been more extensively studied. For that reason, our primary focus in this study was the effect of NH_4VO_3 and NH_4VO_3 + CMC and used the ZnO additive more like a point of comparison. However, when we performed the corrosion experiments, we observed that the three additives' effect is highly dependent on the alloy and can vary from cathodic to mix and anodic. We have observed, for example, that the ZnO additive in Al6062 had almost not anti-corrosive effect. On the other hand, the additives NH_4VO_3 and NH_4VO_3 + CMC showed anti-corrosive activity in all three alloys, making them more versatile. NH_4VO_3 and NH_4VO_3 + CMC are also highly soluble in alkaline medium, making them interesting to use in liquid or gel electrolytes for aluminum-air batteries and give them an advantage over ZnO has more limited solubility. Another important aspect is that NH_4VO_3 based additives helped to make alloys with bad anti-corrosive properties like Al5052 comparable to better alloys like Al6062. According to the hydrogen production tests and the impedance measurements, NH_4VO_3 based additives do not require forming a thick protective layer to decrease the corrosion of the aluminum alloys effectively.

The anti-corrosive layer formed from NH_4VO_3 electrolyte is composed of polymeric forms of tetrahedric vandates with vanadium in +5 oxidation state for the three alloys. However, in some alloys, intermetallic compounds of magnesium with vanadium +5 and polymeric forms of tetrahedral vanadates with +4 oxidation state can also be formed. In the hydrogen production measurements, we

Research article
doi.org/10.1002/elsa.202100125
Chemistry Europe
European Chemical Societies Publishing

observed that adding CMC to the NH_4VO_3 additive might help to reduce the corrosion rate in the Al7475 alloy.

In conclusion, NH_4VO_3 and NH_4VO_3 + CMC additives are up-and-coming anti-corrosive candidates to be used in aluminum-air batteries. Those results deserve more investigation and will be an object of future studies.

4 | EXPERIMENTAL SECTION

4.1 | Reagents

It was used carboxymethylcellulose sodium salt, low viscosity from Sigma–Aldrich. Also, aluminum chloride hexahydrate, molybdenum oxide, ammonium metavanadate, zinc oxide, and sodium hydroxide were >99% purity from Sigma–Aldrich.

4.2 | Preparation of heteropolycompounds

4.2.1 | Synthesis of the Keggin-type heteropolyacid $H_6PMo_{11}AlO_{40}$

The $H_6PMo_{11}AlO_{40}$ was synthesized according to Romanelli.[62] A mixture of H_3PO_4 85% (0.58 g (0.01 mol)), $AlCl_3.6H_2O$ (1.21 g (0.005 mol)), and MoO_3 (14.4 g (0.11 mol)) was suspended in 150 mL of distilled water. The mixture was stirred for 6 h at 80°C. After cooling down to room temperature and removing insoluble polymolybdates, the heteropolyacid solution was evaporated and dried at 85°C for 24 h. After that, yellow crystals of $H_6PMo_{11}AlO_{40}$ were obtained.

4.2.2 | Synthesis of the Keggin type heteropolyacid $H_5PMo_{11}Al_{0.5}V_{0.5}O_{40}$

The $H_5PMo_{11}Al_{0.5}V_{0.5}O_{40}$ was synthesized according to Romanelli.[62] A stoichiometric mixture of 0.58 g (0.01 mol) of H_3PO_4 85%, 0.6 g (0.0025 mol) of $AlCl_3.6H_2O$, 0.22 g (0.0012 mol) of V_2O_5, and 14.4 g (0.11 mol) of MoO_3 was suspended in 150 mL of distilled water. The mixture was stirred for 6 h at 80°C. After cooling down to room temperature and removing insoluble molybdates and vanadates, the heteropolyacid solution was evaporated and dried at 85°C for 24 h. After that, yellow-orange crystals of $H_5PMo_{11}Al_{0.5}V_{0.5}O_{40}$ were obtained.

4.2.3 | Infrared and Raman spectroscopic analyses

The main IR bands of $H_6PMo_{11}AlO_{40}$ were 1060 (P-Oa), 866 (Mo-Ob-Mo), 787 (Mo-Oc-Mo) cm^{-1} and the Raman peaks were 945, 469, 1456, and 1766 cm^{-1}. For the $H_5PMo_{11}Al_{0.5}V_{0.5}O_{40}$, the main IR bands were 1047 (P-Oa), 947 (Mo = Od), 879 (Mo-Ob-Mo), and 736 (Mo-Oc-Mo) cm^{-1} and the Raman peaks were 488, 928, 1464, 1515, and 1764 cm^{-1}. Spectra are shown in the Supporting Information (Figure S32).

4.2.4 | Preparation of materials

Ammonium vanadate 0.5 mol/L, zinc oxide 0.025 mol/L, the heteropolyacid $H_6PMo_{11}AlO_{40}$, and $H_5PMo_{11}Al_{0.5}V_{0.5}O_{40}$ 10 mmol/L were evaluated as anti-corrosive for three commercial aluminum alloys with different metal compositions Al7475, Al6062, and Al5052 in 2 mol/L KOH solution. All experiments were carried out with aluminum samples previously polished. The size of the samples was 20 mm × 10 mm.

4.2.5 | Hydrogen evolution test

Concentrations of additives in alkaline solutions were NH_4VO_3 0.5 mol/L, ZnO 0.025 mol/L, $PMo_{11}AlV_{0.5}$ 10 mmol/L, $PMo_{11}AlV_{0.5}$ 10 mmol/L, NH_4VO_3 0.5 mol/L + CMC 10 g/L. The hydrogen produced by each alloy in 25 mL of 2 mol/L KOH solution with different additives was measured by collecting hydrogen gas. The aluminum samples (area: 4 cm^2) were placed in an airtight container connected to a burette (Figures S33). The total immersion time was 30 min, and the displaced volume of water was read every 5 min. This measurement was repeated twice for each additive with the three alloys.

The hydrogen evolution rate (E_r) over the immersion period was calculated according to Equation (1):

$$E_r = \frac{V_{H_2}}{A \times T} \tag{8}$$

where E_r is in mL cm^{-2} min^{-1}, A is specimen area (in cm^2), V_{H2} is the volume of hydrogen gas collected (in mL), and T is the immersion period (in min). The corrosion rate (C_r) was calculated as follows:

$$C_r = \frac{m_{Al}}{A \times T} \tag{9}$$

where C_r is in mg cm^{-2} min^{-1}, A is specimen area (in cm^2), m_{Al} is the aluminum weight lost during the test (in mg), and T is the immersion period (in min).

Also, the corrosion current (i_{corr}) of the aluminum electrode was calculated according to Equation 10:

$$i_{corr} = i_{H_2} = \frac{2pVF}{RTSt} \tag{10}$$

where p is atmospheric pressure (Pa), V is hydrogen gas volume (cm^3), F is Faraday constant, R is gas constant, T is experimental temperature (K), t is the collecting time (s), and S the electrode area (cm^2).

4.2.6 | Electrochemical measurements

The electrochemical experiments consisted of electrochemical impedance spectroscopy (EIS), and potentiodynamic polarization curves were carried out at 25°C with three electrodes system in a PGSTAT 302N from Metrohm Autolab. The reference electrode was the Ag/AgCl electrode, the counter electrode was a Pt wire, and the working electrode was each of the alloys (exposure area: 0.5 cm^2). As mentioned before the electrolyte was 2 mol/L KOH solution with different additives (Figures S34-S35).

The polarization curves were measured in the potentials from ±400 mV around the corrosion potential at a sweep rate of 0.5 mV/s. The alloy pieces (exposure area: 0.5 cm^2) were immersed in the 2 mol/L KOH-additive solution for 30 min. During this period, the E_{OCP} was measured, and subsequently, the respective polarization curve was carried out. EIS measurements were carried out under the frequency range from 0,01 Hz to 100 kHz at open circuit potential after 30 min immersion, and the sinusoidal voltage amplitude was 0.01 mV.

4.2.7 | Scanning electron microscopy and energy-dispersive X-ray spectroscopy

The alloys samples resulting from the H_2 evolution test were used in the microscopy studies to observe surface morphology and determined the composition of the Al surface after immersion in the electrolytic solution with additives. A Hitachi S-300 scanning electron microscope (SEM) and an energy-dispersive X-ray spectroscopy (EDX) system equipped with an INCAx-sight (Oxford Instruments) were used. The corrosion products were not removed from the Al surface for the measurement.

4.3 | Raman spectroscopic experiments

All Raman spectra in this work were acquired on a WITec Alpha 300R Raman microprobe system. Each of the alloys was immersed in KOH 2 mol/L-NH_4VO_3 0.5 mol/L for 30 min (area: 4 cm^2). After drying the pieces, single Raman spectra were acquired with 532 nm excitation, 20 mW of power, 5 s of integration time, and 100 accumulations. Raman measurements were replicated on three different areas of samples. Also, a 2D area mapping was carried out twice for each piece (points per line: 50 × 50, area: 2500 μm^2).

ACKNOWLEDGMENTS

The authors thank Posgrado en Química, Vicerrectoría de Investigación (UCR), and CONARE (Costa Rica).

DATA AVAILABILITY STATEMENT

The data that support the findings of this study are available from the corresponding author upon reasonable request.

REFERENCES

1. C. Wang, Y. Yu, J. Niu, Y. Liu, D. Bridges, X. Liu, J. Pooran, Y. Zhang, A. Hu, *Appl. Sci.* **2019**, 1.
2. H. Chen, T. N. Cong, W. Yang, C. Tan, Y. Li, Y. Ding, *Prog. Nat. Sci.* **2009**, *19*, 291.
3. G. A. Elia, K. Marquardt, K. Hoeppner, S. Fantini, R. Lin, E. Knipping, W. Peters, J. F. Drillet, S. Passerini, R. Hahn, *Adv. Mater.* **2016**, *28*, 7564.
4. S. M. Rezvanizaniani, Z. Liu, Y. Chen, J. Lee, *J. Power Sources* **2014**, *256*, 110.
5. T. Leisegang, F. Meutzner, M. Zschornak, W. Münchgesang, R. Schmid, T. Nestler, R. A. Eremin, A. A. Kabanov, V. A. Blatov, D. C. Meyer, *Front. Chem.* **2019**, *7*, 268.
6. V. Blay, R. E. Galian, L. M. Muresan, D. Pankratov, P. Pinyou, G. Zampardi, *Adv. Sustain. Syst.* **2020**, *4*, 1900145.
7. M. A. Rahman, X. Wang, C. Wen, *J. Electrochem. Soc.* **2013**, *160*, A1759.
8. J. Ren, J. Ma, J. Zhang, C. Fu, B. Sun, *J. Alloys Compd.* **2019**, *808*, 151708.
9. E. I. Shkolnikov, A. Z. Zhuk, M. S. Vlaskin, *Renew. Sustain. Energy Rev.* **2011**, *15*, 4611.
10. Q. Li, N. J. Bjerrum, *J. Power Sources* **2002**, *110*, 1.
11. Q. Liu, Z. Pan, E. Wang, L. An, G. Sun, *Energy Storage Mater.*. **2020**, *27*, 478.
12. R. Liang, Y. Su, X. L. Sui, D. M. Gu, G. S. Huang, Z. B. Wang, *J. Solid State Electrochem.* **2019**, *23*, 53.
13. Z. Moghadam, M. Shabani-Nooshabadi, M. Behpour, *J. Mol. Liq.* **2017**, *242*, 971.
14. Q. X. Kang, T. Y. Zhang, X. Wang, Y. Wang, X. Y. Zhang, *J. Power Sources* **2019**, *443*, 227251.
15. M. Pino, J. Chacón, E. Fatás, P. Ocón, *J. Power Sources* **2015**, *299*, 195.
16. L. Yang, Y. Wu, S. Chen, Y. Xiao, S. Chen, P. Zheng, J. Wang, J. E. Qu, *Mater. Chem. Phys.* **2021**, *257*, 123787.
17. C. Zhu, H. Yang, A. Wu, D. Zhang, L. Gao, T. Lin, *J. Power Sources* **2019**, *432*, 55.
18. X. Y. Wang, J. M. Wang, Q. L. Wang, H. B. Shao, J. Q. Zhang, *Mater. Corros.* **2011**, *62*, 1149.
19. E. Grishina, D. Gelman, S. Belopukhov, D. Starosvetsky, A. Groysman, Y. Ein-Eli, *ChemSusChem* **2016**, *9*, 2103.
20. B. J. Hopkins, Y. Shao-horn, D. P. Hart, *Science (80-.)* **2018**, *362*, 658.
21. J. B. Wang, J. M. Wang, H. B. Shao, J. Q. Zhang, C. N. Cao, *J. Appl. Electrochem.* **2007**, *37*, 753.
22. W.-H. Lee, S.-R. Choi, J.-G. Kim, *J. Electrochem. Soc.* **2020**, *167*, 110503.

23. D. P. Wang, D. Q. Zhang, K. Y. Lee, L. X. Gao, *J. Power Sources* **2015**, *297*, 464.
24. Q. X. Kang, Y. Wang, X. Y. Zhang, *J. Alloys Compd.* **2019**, *774*, 1069.
25. D. Wang, H. Li, J. Liu, D. Zhang, L. Gao, L. Tong, *J. Power Sources* **2015**, *293*, 484.
26. G. S. Frankel, R. L. McCreery, *Electrochem. Soc. Interface* **2001**, *10*, 34.
27. M. Iannuzzi, J. Kovac, G. S. Frankel, *Electrochim. Acta* **2007**, *52*, 4032.
28. K. Der Aluminiumlegierung, *Mater. Sci. Eng. Technol.* **2017**, 646.
29. D. S. Kharitonov, I. B. Dobryden', B. Sefer, I. M. Zharskii, P. M. Claesson, I. I. Kurilo, *Prot. Met. Phys. Chem. Surfaces* **2018**, *54*, 291.
30. J. J. Chen, M. D. Symes, L. Cronin, *Nat. Chem.* **2018**, *10*, 1042.
31. M. Iannuzzi, T. Young, G. S. Frankel, *J. Electrochem. Soc.* **2006**, *153*, B533.
32. D. S. Kharitonov, C. Örnek, P. M. Claesson, J. Sommertune, I. M. Zharskii, I. I. Kurilo, J. Pan, *J. Electrochem. Soc.* **2018**, *165*, C116.
33. K. D. Ralston, R. G. Buchheit, *ECS Electrochem. Lett.* **2013**, *2*, C35.
34. M. Hutin, M. H. Rosnes, D. L. Long, L. Cronin, *Polyoxometalates: Synthesis and Structure - From Building Blocks to Emergent Materials*, Elsevier Ltd., **2013**.
35. E. Assady, B. Yadollahi, M. Riahi Farsani, M. Moghadam, *Appl. Organomet. Chem.* **2015**, *29*, 561.
36. W. Qi, L. Wu, *Polym. Int.* **2009**, *58*, 1217.
37. Q. Li, L. Zhang, J. Dai, H. Tang, Q. Li, H. Xue, H. Pang, *Chem. Eng. J.* **2018**, *351*, 441.
38. X. Zhu, H. Yang, Y. Cao, X. Ai, *Electrochim. Acta* **2004**, *49*, 2533.
39. R. K. Gupta, N. L. Sukiman, K. M. Fleming, M. A. Gibson, N. Birbilis, *ECS Electrochem. Lett.* **2012**, *1*, C1.
40. N. Birbilis, R. G. Buchheit, *J. Electrochem. Soc.* **2005**, *152*, B140.
41. M. Q. I. Polmear, D. StJohn, J.-F. Nie, *Wrought Aluminium Alloys*, Elsevier Ltd., **2017**.
42. D. S. Kharitonov, J. Sommertune, C. Örnek, J. Ryl, I. I. Kurilo, P. M. Claesson, J. Pan, *Corros. Sci.* **2018**, *148*, 237.
43. D. S. Kharitonov, J. Sommertune, C. Örnek, J. Ryl, I. I. Kurilo, P. M. Claesson, J. Pan, *Corros. Sci.* **2019**, *148*, 237.
44. M. Aureliano, C. A. Ohlin, M. O. Vieira, M. P. M. Marques, W. H. Casey, L. A. E. Batista De Carvalho, *Dalt. Trans.* **2016**, *45*, 7391.
45. J. L. Zhang, J. T. Hu, L. F. Zhang, *Chinese J. Chem. Phys.* **2016**, *29*, 425.
46. G. T. Went, S. T. Oyama, A. T. Bell, *J. Phys. Chem. 94*, **1990**, 4240.
47. T. Kharlamova, E. Sushchenko, T. Izaak, O. Vodyankina, *Catal. Today* **2016**, *278*, 174.
48. J. J. Freeman, A. Wang, K. E. Kuebler, B. L. Jolliff, L. A. Haskin, *Can. Mineral.* **2008**, *46*, 1477.
49. L. E. Firment, H. E. Bergna, D. G. Swartzfager, P. E. Bierstedt, M. L. Van Kavelaar, *Surf. Interface Anal.* **1989**, *14*, 46.
50. D. W. Matson, S. K. Sharma, J. A. Philpotts, *Am. Mineral.* **1986**, *71*, 694.
51. R. Gaggiano, P. Moriamé, M. Biesemans, I. De Graeve, H. Terryn, *Surf. Coatings Technol.* **2011**, *206*, 1269.
52. R. C. Mccune, *Corros. Sci.* **1982**, *22*, 1049.
53. O. Lopez-Garrity, G. S. Frankel, *Electrochim. Acta* **2014**, *130*, 9.
54. J. Liu, D. Wang, D. Zhang, L. Gao, T. Lin, *J. Power Sources* **2016**, *335*, 1
55. C. Engineering, I. Chemistry, *J. Appl. Electrochem.* **1994**, *24*, 772.
56. P. Deepa, R. Padmalatha, *Arab. J. Chem.* **2017**, *10*, S2234.
57. P. D. Reena Kumari, J. Nayak, A. Nityananda Shetty, *Arab. J. Chem.* **2016**, *9*, S1144.
58. E. Naderi, A. H. Jafari, M. Ehteshamzadeh, M. G. Hosseini, *Mater. Chem. Phys.* **2009**, *115*, 852.
59. G. M. Tomboc, P. Yu, T. Kwon, K. Lee, J. Li, *APL Mater.* **2020**, *8*, 050905.
60. N. Imanishi, O. Yamamoto, *Mater. Today Adv.* **2019**, *4*, 100031.
61. J. Li, F. Yan, Z. Su, T. Zhang, X. Zhang, H. Sun, *J. Electrochem. Soc.* **2020**, *167*, 090529.
62. G. P. Romanelli, D. O. Bennardi, V. Palermo, P. G. Vázquez, *Lett. Org. Chem. 4*, **2007**, 544.

SUPPORTING INFORMATION

Additional supporting information may be found online in the Supporting Information section at the end of the article.

How to cite this article: A. P. Atencio, J. R. Aviles, D. Bolaños, R. Urcuyo, M. L. Montero, D. González-Flores, P. Ocón, *Electrochem. Sci. Adv.* **2021**, e2100125.
https://doi.org/10.1002/elsa.202100125